Mixing and pumping by pairs of helices in a viscous fluid

Amy Buchmann, Lisa J. Fauci, Karin Leiderman, Eva Strawbridge, and Longhua Zhao

Phys. Rev. E **97**, 023101 — Published 1 February 2018

DOI: 10.1103/PhysRevE.97.023101

Mixing and pumping by pairs of helices in a viscous fluid

Amy Buchmann* and Lisa J. Fauci†
Department of Mathematics, Tulane University, New Orleans, LA, USA

Karin Leiderman‡
Department of Applied Mathematics and Statistics, Colorado School of Mines, Golden, CO, USA

Eva Strawbridge§
Department of Mathematics and Statistics, James Madison University, Harrisonburg, VA, USA

Longhua Zhao¶
Department of Mathematics, Applied Mathematics, and Statistics,
Case Western Reserve University, Cleveland, OH, USA
(Dated: November 25, 2017)

Here we study the fluid dynamics of a pair of rigid helices rotating at a constant velocity, tethered at their bases, in a viscous fluid. Our computations use a regularized Stokeslet framework, both with and without a bounding plane, so we are able to discern precisely what flow features are unaccounted for in studies that ignore the surface from which the helices emanate. We examine how the spacing and phase difference between identical rotating helices affects their pumping ability, axial thrust, and power requirements. We also find that optimal mixing of the fluid around two helices is achieved when they rotate in opposite phase, and that the mixing is enhanced as the distance between the helices decreases.

I. INTRODUCTION

Rotating helical flagella attached to a cell body are the propellers responsible for the locomotion of most bacteria. Driven by molecular motors at their base, the helices rotate, leading to hydrodynamic forces that propel the cell [1]. If the cell body was tethered, the rotating helices would act to stir and pump the nearby viscous fluid. Harnessing the action of these naturally actuated filaments within a microfluidic device was put forth as an intriguing possibility for fluid transport and mixing by bacterial carpets [2]. Flagellar rotation could be maintained for quite some time without the need for an external power source [3]. Alternatively, fabricated helical micromachines that are actuated by an imposed magnetic field could also serve as microscale mixers [4]. In either case, in order to control or quantify fluid transport and mixing, the flow features around the rotating helices should be understood.

In the past decades, there has been considerable analysis of propulsion by helical flagella. Because viscous forces dominate inertial forces at the microscale, the hydrodynamics of bacterial locomotion in a Newtonian fluid is well-described using the Stokes equations. The linearity of these equations and the slenderness of the helical filament allow for the use of methods such as resistive force theory [5], slender body theory [6], or regularized Stokeslets [7]. Rodenborn et al. [8] performed coordinated physical experiments and computations that measured the axial thrust and torque on rotating rigid helices of different geometries. They showed that slender body theory and regularized Stokeslets calculations agreed with laboratory measurements within experimental uncertainty, while resistive force calculations showed significant differences for helices with small pitch relative to radius. In addition to models of free swimming due to the prescribed kinematics of a rigid helix and a counter-rotating cell body, other studies examine the elastohydrodynamic coupling between shape deformation of the helix and the fluid [1, 9]. Moreover, both physical and computational experiments have shown that bundling of nearby helical flagella occurs due to hydrodynamic forces [10–15].

The presence of nearby surfaces has an effect on microorganism motility. A free-swimmer driven by a helical flagellum and a counter-rotating cell body will swim in circular rather than straight trajectories near a planar surface [16]. Naturally, it is to be expected that the flow structures around rotating helices emanating from a planar wall will be affected by the wall's no-slip boundary condition. Recent advances in particle imaging velocimetry have allowed the visualization of flow fields around a single rotating helix at low Reynolds number [17]. Slender body theory was used to compute flows around a pair of helices rotating in free space [18]. Following our computational model of bacterial carpets [19], here we use a regularized Stokeslet framework to examine the fluid flow around a pair of identical rotating helices emanating from a planar wall. The helices are rigid, their axes are perpendicular to the wall, and their rotational velocities are specified. We ask the following simple questions:

* abuchman@tulane.edu
† fauci@tulane.edu
‡ kleiderman@mines.edu
§ strawbem@jmu.edu
¶ lxz315@case.edu

How does the spacing between the helices and their relative phase difference influence their pumping ability? How does the spacing between the helices and their relative phase difference influence the mixing of the nearby fluid? How does the presence of the planar wall affect axial thrust and flow features? We expect that the answers to these simple questions will provide insight into flows driven by helices and the design of microfluidic mixing devices.

II. METHODS

A. Fluid

The motion of an incompressible Newtonian fluid, when inertial forces are negligible, is described by the Stokes equations:

$$-\nabla p + \mu \Delta \mathbf{u} = \mathbf{F} \tag{1}$$

$$\nabla \cdot \mathbf{u} = 0, \tag{2}$$

where p is fluid pressure, $\mathbf{u}$ is fluid velocity, μ is fluid viscosity, and $\mathbf{F}(\mathbf{x})$ is a force density representing the force of the helices on the fluid.

Following our previous model of a fluid-helix system [19], we choose a regularized Stokeslet formulation [7] where forces are distributed along the centerline of the helices [20]. Rather than assuming that these are point-forces, the force density concentrated at a point $\mathbf{x}_k$ is assumed to be

$$\mathbf{F}_k(\mathbf{x}) = \mathbf{f}_k \phi_\epsilon(||\mathbf{x} - \mathbf{x}_k||) \tag{3}$$

where $\mathbf{f}_k$ is a vector coefficient and ϕ_ϵ is a smooth approximation of a Dirac delta function (also known as a blob function). Here, we use the following functional form:

$$\phi_\epsilon(r) = \frac{15\epsilon^4}{8\pi(r^2+\epsilon^2)^{7/2}}.$$

We interpret the regularization parameter ϵ as a physical parameter that represents the radius of the filament that is wound into a helix [21].

For a single point force density of strength $\mathbf{f}_0$ located at $\mathbf{x}_0$, the induced velocity $\mathbf{u}$ at any point $\mathbf{x}$ can be written in terms of the regularized Stokeslet, $\mathcal{S}_\epsilon(\mathbf{x}, \mathbf{x}_0)$, such that

$$\mathbf{u}(\mathbf{x}) = \frac{1}{8\pi\mu}\mathcal{S}_\epsilon(\mathbf{x}, \mathbf{x}_0)\mathbf{f}_0(\mathbf{x}_0).$$

Using the definitions for the regularized solutions to the biharmonic and Laplace equation in three dimensions [7]

$$\Delta^2 B_\epsilon(r) = \Delta G_\epsilon(r) = \phi_\epsilon(r),$$

where $r = ||\mathbf{x} - \mathbf{x}_0||$, it follows that

$$\begin{aligned}\mathcal{S}_\epsilon(\mathbf{x}, \mathbf{x}_0) &= (-\Delta \mathbf{I} + \nabla\nabla)B_\epsilon(r), \\ &= H_1(r)\mathbf{I} + H_2(r)(\mathbf{x}-\mathbf{x}_0)(\mathbf{x}-\mathbf{x}_0),\end{aligned}$$

where $H_1(r)$ and $H_2(r)$ are

$$H_1(r) = -\frac{B'_\epsilon(r)}{r} - B''_\epsilon(r), \qquad H_2(r) = \frac{rB''_\epsilon(r) - B'_\epsilon(r)}{r^3}.$$

Thus, by linearity of the Stokes equations and using our regularized delta function, the velocity $\mathbf{u}$ at any point $\mathbf{x}$ due to a set of forces $\mathbf{f}_k$ located at positions $\mathbf{x}_k$ is

$$\mathbf{u}(\mathbf{x}) = \sum_{k=1}^{2M}\left[\frac{\mathbf{f}_k(r_k^2+2\epsilon^2) + (\mathbf{f}_k \cdot (\mathbf{x}-\mathbf{x}_k))(\mathbf{x}-\mathbf{x}_k)}{8\pi\mu(r_k^2+\epsilon^2)^{3/2}}\right] \tag{4}$$

where $r_k = |\mathbf{x} - \mathbf{x}_k|$ and M is the number of forces along each of the two helical centerlines.

Note that this velocity resulting from $2M$ concentrated forces is defined everywhere, is an exact solution of the Stokes equations in three dimensions, and is exactly incompressible. In particular, if we evaluate Equation (4) at the $2M$ points $\mathbf{x}_k$, we have a $6M \times 6M$ linear system that relates the forces $\mathbf{f}_k$ applied at the points of each helix to the velocities $\mathbf{u}_k$ at those points. Because in this work we specify the kinematics of the helices, the velocities are known, and we solve this linear system for the forces that must be exerted along the helices to achieve these kinematics. Once these forces are known, Equation (4) may be used to evaluate the fluid velocity at any point in space.

For flows bounded by a plane, the boundary condition $\mathbf{u} = 0$ at the plane must be enforced. Within the context of regularized forces, this is done by placing a regularized Stokeslet, doublet, dipole and rotlet at the image point. The details of the regularized image system are described in [22]. The regularized Stokeslet method has been used to simulate flows at the microscale in applications including hyperactivated sperm motility [21], nodal cilia flow in embryology [23], optimal cilia design [24] and synchronization of waving elastic filaments [25]. The validation of this method using theory as well as comparison of results with those of other numerical methods or experiments has also been addressed, for example [7, 20, 26].

B. Helical Flagella

Figure 1 shows the configuration of two upright helices whose axes (of length L) are parallel, placed a distance d apart. The helices are identical, rotate in the same direction, but could have a fixed phase difference. Figure 1 also depicts zoomed-in circular projections of each of the helices onto the $z = 0$ plane that indicate the helical radius α and the phase difference ϕ.

The centerline of a helical flagellum $\mathbf{x}_c = (x_c, y_c, z_c)$ is parameterized by s, where $0 \le s \le L$:

$$\begin{aligned}x_c(s) &= \alpha \tanh(\tau s)\cos\left(\frac{2\pi s}{\lambda} + \phi\right) \\ y_c(s) &= \alpha \tanh(\tau s)\sin\left(\frac{2\pi s}{\lambda} + \phi\right) \\ z_c(s) &= s.\end{aligned} \tag{5}$$

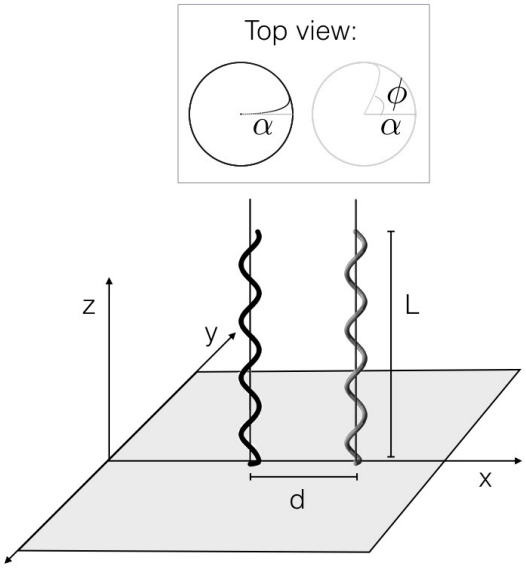

FIG. 1. Sketch of two upright helices. The axis of each helix has length L, the radius of the helix is α, and the fraction L/λ, where λ is the pitch. Both helices rotate counter-clockwise from the top view, but with a phase difference ϕ. d is the distance between the helices.

Here λ is the helical pitch, τ is a tapering parameter that allows the radius of the helix to approach zero at its base, ϕ is the phase angle, α is the radius of the helix. The pitch angle, β, is related to the helical pitch by

$$\tan\beta = \frac{2\pi}{\lambda}\alpha. \tag{6}$$

The time-dependent position of the centerline of an upright helix rotating with specified angular velocity $(0, 0, \omega)$ is:

$$\mathbf{x}(t) = R_\omega \mathbf{x}_c, \tag{7}$$

where

$$R_\omega = \begin{bmatrix} \cos(\omega t) & -\sin(\omega t) & 0 \\ \sin(\omega t) & \cos(\omega t) & 0 \\ 0 & 0 & 1 \end{bmatrix}.$$

Following the physical experiments of Zhong *et al.* [17], we fix the geometry of the helices to be left-handed and to have a radius to axial length ratio close to the typical values for *Escherichia coli* bacteria. In particular, in non-dimensional units, we choose $\mu = 1$, the radius of the filament to be $\epsilon = 0.01$, the axial length of the helix to be $L = 2.2$, and the radius of the helix to be $\alpha = 0.085$. In most of the studies presented below, we choose a pitch angle of $\beta = \pi/4$ radians and a tapering parameter of $\tau = 1000$. In addition, we vary the distance between the centerline of the helices d (see Figure 1) from 0.25 to 2.5, which represents a range of approximately 3 helix radii (3α) to 30 helix radii (30α).

III. RESULTS

A. A single helix

An untethered helix, externally-actuated to rotate about its axis, would translate in a viscous fluid. The direction of translation would depend upon the handedness of the helix and the direction of rotation. If the forward motion of such a helix was disallowed by tethering it at its base, it would produce thrust in the axial direction. Moreover, in addition to causing the nearby fluid to rotate as it rotates around its axis, the helix acts as a pump, generating a net flow away from its base [19]. In recent physical experiments, Zhong *et al.* [17] examined the flow field around a single rotating helix at low Reynolds number using particle imaging velocity. The PIV measurements were taken on a plane that contained the axis of the helix, and phase-averaged velocity data was projected in this plane. Choosing the same helical geometry as in [17] and stated above, Figure 2 shows the velocity field, contours of the transverse velocities (positive indicates pointing to the right), contours of the axial velocities and contours of vorticity in a bisecting plane of the helix using regularized Stokeslets with images due to a wall. In particular, each helical centerline was discretized using $M = 158$ equally spaced points, and we evaluated the velocity field on a uniform 50×50 grid in the plane using Equation (4). In Figure 2, we choose the same conventions as the corresponding PIV figures in [17], noting that the left-handed helix is rotated counterclockwise when viewed from above. As in [17], we see that transverse velocity alternates sign as the three-dimensional segments of the helix move in or out of the plane as it rotates (panel B), the axial velocity is always downward (panel C) and vorticity concentrates at the peaks of the projection of the helix onto the plane. The transverse and axial velocities were normalized by $\alpha\omega$.

Zhong *et al.* [17] investigated the thrust production of the rotating helices as a function of the pitch angle. The total axial length of the helix L and the radius α were kept fixed, but the pitch angle in Equation (6) was varied. As the pitch angle gets larger, the helix becomes more tightly wound and more turns about the axis comprise the helix. In a series of experiments of helices with pitch angles varying from fifteen to nearly seventy degrees rotated at eight different frequencies, Zhong *et al.* [17] reported the normalized thrust $T/(\mu\omega\alpha L)$. The helix was mounted vertically, and was immersed in the rectangular tank attached to the shaft of a micro-gear motor, and the thrust was recorded using a force sensor. The physical experiments indicated that the maximum thrust was achieved near pitch angle $\beta = 45$ degrees. Resistive force calculations to measure thrust were performed using the coefficients proposed by Gray and Hancock [5], Cox [27] and Lighthill [6]. Resistive force theory is a local theory that considers the slender filament to be made up of individual cylindrical elements, and relates the velocity and force on the elements by resistance coefficients. The

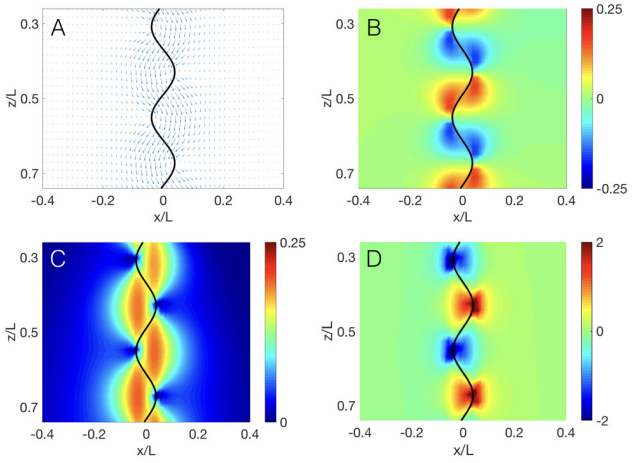

FIG. 2. (A) Velocity field around a portion of a helix projected onto a bisecting plane (B) transverse velocity contours (C) axial velocity contours (D) vorticity contours. These computational results should be compared with the experimental results shown in Figure 2 of [17].

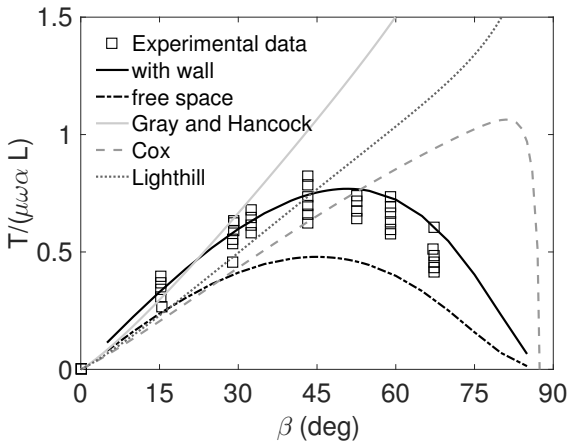

FIG. 3. Normalized thrust as a function of pitch angle. Experimental data adapted from Figure 8 of [17] (squares), theoretical calculations using approximations by Gray and Hancock [5] (grey solid line), Cox [27] (grey dashed line), and Lighthill [6] (grey dotted line), our regularized Stokeslet calculations in the presence (black solid line) and absence (black dash-dot line) of a no-slip wall. The RFT calculations do not account for a bounding plane. Our simulations in the presence of a wall show very good agreement with the experimental data.

interaction between local elements through the fluid is ignored. Figure 3 shows the experimental data and resistive force calculations adapted from Figure 8 of [17] along with the regularized Stokeslet calculations, both in free-space (dotted black curve) and with a wall (solid black curve). We see that for small pitch angles, the resistive force theories and experiments show agreement. However, these approximations do not capture the experimental results as pitch angle increases. In contrast, the regularized Stokeslet calculations demonstrate that maximum axial thrust is achieved near $\beta = 45$. We also see that the the thrust for all pitch angles is greater when the helix is emanating from a wall, and that the inclusion of the wall more closely matches the experimental data, where the helix is emanating from a motor apparatus [17].

B. Two helices

1. *Flow induced by two rotating helices*

We begin with simulations of flow around two rotating helices that are in free-space (Figure 4) or tethered to a wall (Figure 5). In both cases, the helices are upright and self-rotating with frequency 1 Hz. Figures 4 and 5 show snapshots of passive tracer particles in the flow, initialized on the horizontal plane $z = 0.5$. The tracer colors indicate height; from dark blue to red is low to high. Figure 4 shows that in the absence of a wall tracer particles are pushed up and outward, away from the helices. In contrast, the presence of the wall (Figure 5) leads to dramatically different flows where the tracers are first drawn in horizontally toward the helices, then swirl around the helices while moving upward and staying close to the helices; it is not until the tracers are above the helices that they begin to expand in the outward direction. Comparing the colors (heights) of the tracers in Figures 4 and 5 we see that the tracers have reached greater heights in the absence of the wall after the same amount of time.

To see how the phase difference between the helices affects the flow field, we computed the vertical and transverse velocity profiles as well as the vorticity for two helices in free-space (not shown) and tethered to a wall, (see Figure 6), for three phase differences. In all of these simulations, the distance between the helices is fixed at 3α and the rotational frequency is fixed at 1 Hz. For the computations in free-space, the transverse and vertical velocities for two helices rotating in phase compare well qualitatively to the experimental and computational results reported by Kim and Powers [29].

For simulations of two helices tethered to a wall, the columns of Figure 6 show instances where the helices are in phase (left), out of phase by $\pi/2$ (middle), and π (right). In all panels, we show the velocity components in a vertical plane through the middle of the helices. Panels G-I show that as helices vary from being in phase to being out of phase by π, the vertical component of the velocities *between* the helices increases. In contrast, the transverse velocities in panels D-F decrease with larger phase difference. In addition, the sign of the vorticity in a horizontal slice through the helices switches from being the same sign when the helices are in phase (panel J) to opposite sign when the helices are out of phase (panel L).

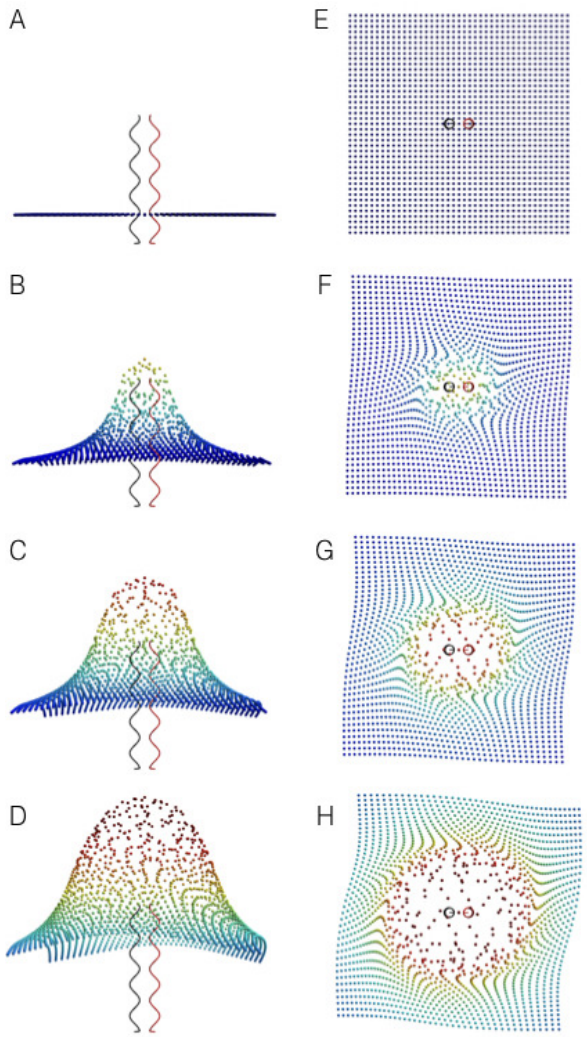

FIG. 4. Snapshots of fluid particles in the flow generated by two rotating helices in free space. Side views (A-D) and top views (E-H) at $t = 0$, 20, 40 and 70. Geometries are the same as in the single helix case from Zhong *et al.*[17], with pitch angle $\beta = 45^o$. The bases of the helices are located at $(-2\alpha, 0, 0)$ and $(2\alpha, 0, 0)$, the phase difference is π, colors indicated height. (See Supplementary Materials [28] for movies.)

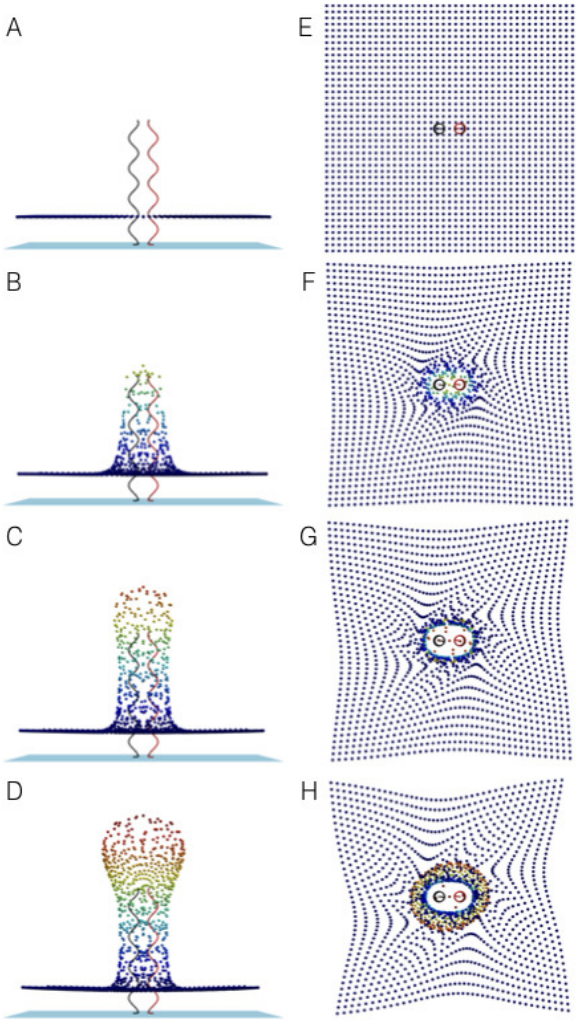

FIG. 5. Snapshots of fluid particles in the flow generated by two rotating helices tethered to a wall. Side views (A-D) and top views (E-H) at $t = 0$, 20, 40 and 70. Geometries are the same as in the single helix case from Zhong *et al.*[17], with pitch angle $\beta = 45^o$. The bases of the helices are located at $(-2\alpha, 0, 0)$ and $(2\alpha, 0, 0)$, the phase difference is π, colors indicated height. The blue plane is the location of the no-slip wall at $z = 0$. (See Supplementary Materials [28] for movies.)

2. *Thrust, power and flux*

Two characteristic quantities of interest are the thrust generated by the helices and the power required to attain their prescribed motion. Each of these quantities is computed for a single helix in the presence of the other helix, averaged over one single rotation, and normalized by the same quantity computed for a single helix in isolation. We examine how both thrust and power depend upon phase and separation distance when the tethered helices rotate in free-space or in the presence of a planar wall.

The total thrust is the integral of the $z-$component of the force along the centerline of the helix of interest. For an isolated helix with geometric parameters as above, the average thrust it generates over one period tethered to a wall is enhanced by 46% compared to the thrust generated in free-space (data not shown). This enhancement is in accord with the results shown Figure 3 for the case when $\beta = 45^o$, comparing the thrust computed in free-space (dash-dot black line) to that with a wall (solid black line). When a second helix (call it h_2) is placed in the same fluid domain as the first helix (call it h_1) we compute the thrust generated by h_1 in the presence of h_2, averaged over one rotation, and normalize it by the thrust generated by h_1 in the absence of h_2.

Panels A and B in Figure 7 show the thrust generated by helices tethered to a wall, as a function of phase dif-

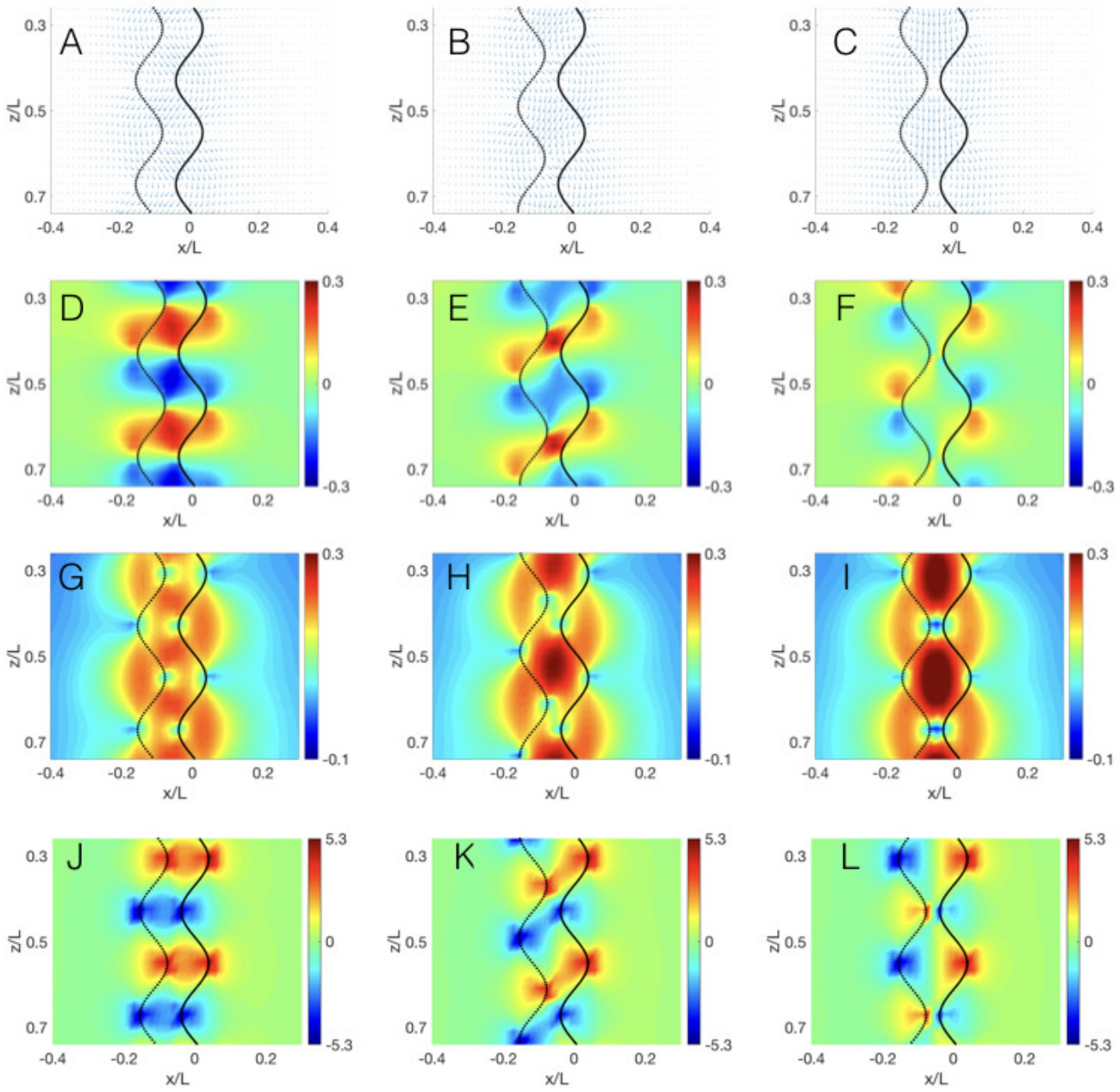

FIG. 6. Instantaneous velocity field (A-C), transverse (D-F) and vertical velocities (G-I), and vorticity (J-L) for two helices tethered to a wall. The separation distance is 3α, they are rotating at 1 Hz, and they are either in phase (left column), out of phase by $\pi/2$ (middle column) or out of phase by π (right column).

ference and separation distance, respectively. In panel A we see that it is only when the helices are very close that the phase difference has an effect on thrust. In particular, when $d = 0.25$, the maximum thrust results when $\phi = \pi$ and they are completely out of phase. For any fixed phase difference, however, the thrust increases to the value in isolation, as the helices become farther apart, as seen in panel B.

Panels C and D in Figure 7 show the thrust generated by helices in free-space, as a function of phase difference and separation distance, respectively. Again we see that the thrust generated by a helix in isolation is greater than the thrust generated by either of two helices together. This behavior compares well with axial force measurements on two rotating helices in free space using slender body theory [18]. Whether rotating in free space or tethered to a wall, the thrust generated by a single helix of a pair will approach the thrust it would

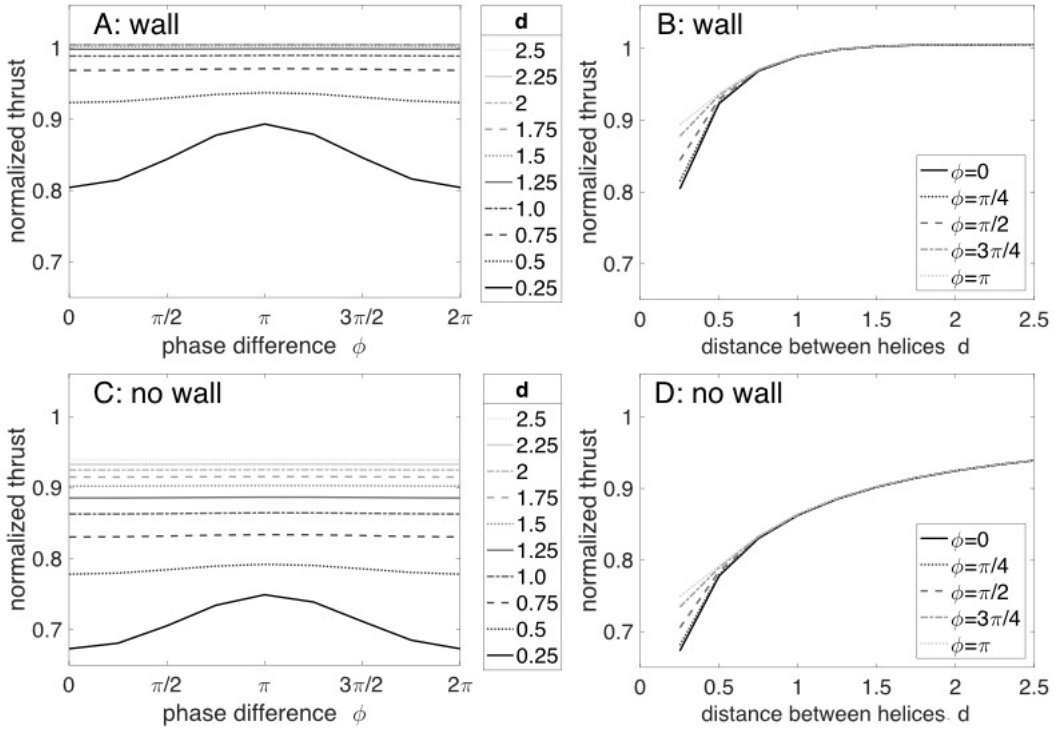

FIG. 7. Normalized thrust generated by two helices in the presence of a wall (A,B) and in free space (C,D). Thrust is shown as a function of phase difference (A,C) and separation distance (B,D) between the two helices.

generate in isolation as the distance between the helices increases. Note that in free-space the interaction between helices is $O(R^{-1})$ where R is the distance between them. However, the addition of Stokeslet images in the case of a planar wall results in a $O(R^{-2})$ interaction [30]. Comparing panels B and D demonstrates this - as the separation distance increases between two helices in free-space (panel D), the normalized thrust approaches one much more slowly than when they are tethered to a wall (panel B).

The power required for a single helix to achieve its prescribed motion is the integral of $\mathbf{f} \cdot \mathbf{u}$ along its centerline. For our model (isolated) helix, the required power for it to rotate in free-space is about 3% less than that required if it was tethered to a wall (data not shown). This slight deviation is mainly due to a difference in the $x-$ and $y-$components of the force near the location of the base of the helix (closest to the wall). The $z-$component of force, used to compute thrust above, does differ considerably when the wall is present, but does not factor into the power calculations because material points of the helix rotate parallel to the wall (the $z-$component of velocity is zero).

Similar to the calculation for thrust, we compute the power expended by h_1 in the presence of h_2, averaged over one rotation, and normalized by the the power expended by h_1 in the absence of h_2. Figure 8 shows the normalized power expended by one single helix in the presence of another as a function of phase difference and separation distance, in free-space and with a wall. The first observation is that as the separation distance increases, the power expended by one helix in the pair quickly approaches that of an identical helix in isolation, both in free-space (panel D) and with a wall (panel B). However, when the helices are close ($d = 0.25$) we can see that more power is required when they are completely out of phase ($\approx 6\%$, $\phi = \pi$) and less power required when completely in phase ($\approx 4\%$, $\phi = 0$) when compared to the single helix in isolation.

This reduction in the power requirement for helices rotating in phase is related to the dynamic synchronization of bacterial flagella and the subsequent formation of bacterial flagellar bundles. In the simulations presented here, the phase of rotation of each helix is prescribed as is its rigid geometry. However, in previous models that examine flagellar synchronization, the torque applied at the base of each helix is prescribed, rather than its phase [13–15]. Even if there was a non-zero initial phase difference between these helices, the hydrodynamic coupling results in synchronization, minimizing power required. The speed of synchronization depends upon the distance between helices, the torque strength, and the bending rigidity of the helices [14]. The synchronization of neighboring helices occurs on a faster timescale than the formation of the flagellar bundle [15].

Finally, recognizing that a tethered, rotating helix

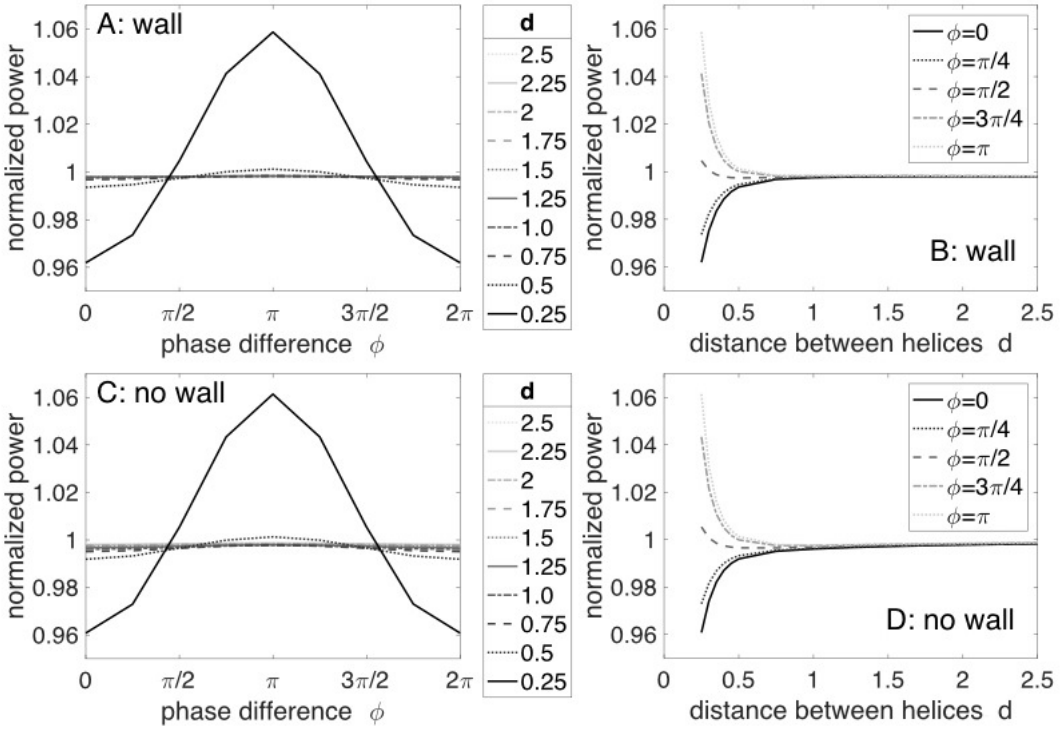

FIG. 8. Normalized power from two helices in the presence of a wall (A,B) and in free space (C,D). Power is shown as a function of phase difference (A,C) and separation distance (B,D) between the two helices.

serves to pump fluid upward away from its base, we examine the flux of fluid that is pushed through a flow meter placed just above it. The flow meter is the square patch, [-5,5] × [-5,5] at a height $z = 2.5$, which is parallel to the $xy-$plane and perpendicular to the axis of the helix whose base is at the origin. The patch is discretized into a regular lattice with spacing $\Delta x = 0.05$, $\Delta y = 0.05$, and Equation (4) is used to evaluate the $z-$velocity at these lattice points. With this surface discretization, we are able to compute the total mass of fluid that passes up through this flow meter in a single rotation of the helix. We now ask the question, do two helices pump twice as much fluid as one? Whether or not these helices are emanating from a wall, the fluid domain is unbounded, and we are calculating the flux past a finite-sized flow meter. For this reason, we examine the mass flux through this flow meter for two helices that are placed sufficiently close together so they still remain well under the rectangular patch. In particular, we choose two pairs of helices with distances $d = 0.25$ and $d = 0.5$ so that their bases are at $(-0.125, 0, 0), (0.125, 0, 0)$ and $(-0.25, 0, 0), (0.25, 0, 0)$, respectively.

We define the normalized flux shown in Figure 9 as one half of the mass of fluid pumped across the flow meter by the two helices during one rotation divided by the mass of fluid pumped across the flow meter by an identical isolated helix. If this normalized flux was equal to one, we would assert that two helices pump twice as much fluid as one. Figure 9 shows that, indeed, this is not the case. Whether or not the helices are tethered to a wall, this normalized flux is less than one independent of the phase difference between them. The neighboring helices are, in effect, competing for the same available fluid to transport up across the flow meter. In fact, the normalized flux for a helix in the closer pair ($d = .25$) is considerably less than that for a helix in the pair placed further apart ($d = .5$), where there is less competition for their nearby fluid. We also note, like the thrust, that the normalized flux is maximized when the helices rotate completely out of phase ($\phi = \pi$) and is greater in the presence of the wall.

3. Mixing

A pair of rotating helices causes the nearby fluid particles to swirl and translate. Here we examine how fluid particles get mixed by the action of these helices, and how this mixing depends upon distance and phase differences between the helices. For instance, Panels A and B of Figure 10 show snapshots at time $t = 0$ of a pair of helices in the same phase tethered to a wall surrounded by a collection of particles of two different colors. Panels C and D of Figure 10 show these particles after 20 rotations of the helix. In order to quantify the mixing of these magenta and green particles, we use a mixing measure $0 \leq M \leq 1$

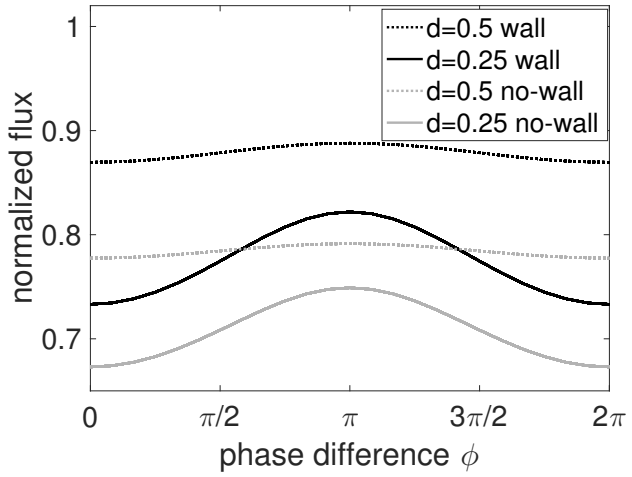

FIG. 9. Normalized flux of fluid passing through a flow meter [-5,5]×[-5,5] at height $z = 2.5$ for two pairs of helices at distances $d = 0.25$ and $d = 0.5$ when either emanating from a wall or rotating in free-space as a function of phase difference. The normalized flux is one half of the mass of fluid pumped across the flow meter by the two helices during one rotation divided by the mass of fluid pumped across the flow meter by an identical isolated helix.

proposed by Robinson *et al.* to evaluate the effectiveness of industrial mixers [31]. While their mixing measure generalizes to more than two particle types (colors), here we describe it in the context of two. Briefly, imagine two different 'types' of tracer particles are placed in a fluid within the region of interest in equal amounts (one half are magenta and one half are green). At any given time, for any spatial point in the domain, one can query how many particles of each color fall within a ball of a given radius centered at that point. If half of the particles in that ball are green and half are magenta, the original global ratios of each color, then locally at that point, the fluid can be considered totally mixed ($\hat{M} = 1$). If, on the other hand, all the particles in that ball are green (or magenta), there is no mixing ($\hat{M} = 0$). This measure, then, depends upon two choices: (1) the spatial centers of these balls, and (2) the radius of these balls. Robinson *et al.* choose a Lagrangian approach whereby the centers of these balls at time t are the positions of the fluid tracers themselves [31]. The choice of the radius should be linked to the spatial scale of the flow, and here we choose each ball radius to be the radius of the helix α.

Consider the vector with two components, where the first component indicates the original (or global) fraction of magenta particles and the second indicates the fraction of green particles. If the space was seeded with an equal amount of each color particles, this vector is $(1/2, 1/2)$. The normalized global fraction vector is then:

$$\mathbf{s}_g = \frac{1}{\sqrt{2}}(1,1)\,.$$

We define a normalized vector of local ratios in a ball of radius α centered at particle p at time t as:

$$\mathbf{s}_l(p,t) = \frac{1}{\sqrt{\left(\frac{n_1}{N_1}\right)^2 + \left(\frac{n_2}{N_2}\right)^2}}\left(\frac{n_1}{N_1}, \frac{n_2}{N_2}\right)$$

where n_1 and n_2 are the number of magenta and green particles, respectively, within the ball and N_1 and N_2 are the total number of green and magenta particles in the whole domain, respectively, at time $t = 0$. Again, here we assume $N_1 = N_2$.

A measure of mixing $\hat{M}(p,t)$ at each particle p (the center of the ball) at time t that has the desired features is then:

$$\hat{M}(p,t) = \frac{\mathbf{s}_l(p,t)\cdot\mathbf{s}_g - M_{min}}{1 - M_{min}}.$$

where $M_{min} = 1/\sqrt{2}$.

Because $\hat{M}(p,t)$ is now a Lagrangian function defined at a tracer particle, we can also visualize the evolution of this mixing measure at the particles. Panels E and F of Figure 10 show a snapshot of particles at time $t = 0$ colored by their mixing measure $\hat{M}(p,0)$, where $\hat{M} = 0$ corresponds to dark blue and complete mixing, $\hat{M} = 1$, corresponds to yellow. Initially, only the particles near the boundary between the magenta and green particles are the centers of balls with non-zero $\hat{M}$, but the particles away from this boundary are centers of balls containing particles of only one color. Whereas a particle always retains its green or magenta color, $\hat{M}(p,t)$ changes over time thus a single particle in the plots that track mixing will change color accordingly. Panels G and H of Figure 10 show the final mixing values of each particle after 20 rotations. Here we see that significant mixing of the two particle types occurred within the central region between the helices.

We now compute this mixing measure for various phase differences and separation distances between the two helices. In each simulation, the domain is seeded with an equal amount of green and magenta particles ($N_1 = N_2 = 5000$), and the boundary between them is equidistant from the base of both helices. We track the mixing measure $\hat{M}(p,t)$ over the course of 20 rotations of the helices.

Snapshots (all from the top view) from some of these simulations are shown in Figure 11. Helices are separated by a distance of $d = 3\alpha$ in the top row and $d = 6\alpha$ in the bottom row. The first column shows the helices and the particles at $t = 0$. Within each column, the phase difference remains the same: $\phi = 0$ (second column), $\phi = \pi/2$ (third column), and out of phase $\phi = \pi$ (fourth column). Subsequent columns show the final particle positions after 20 rotations. When $d = 3\alpha$, we observe significant mixing near the helices. As d increases, the mixing appears to decrease; for $d = 6\alpha$, the particles inside each

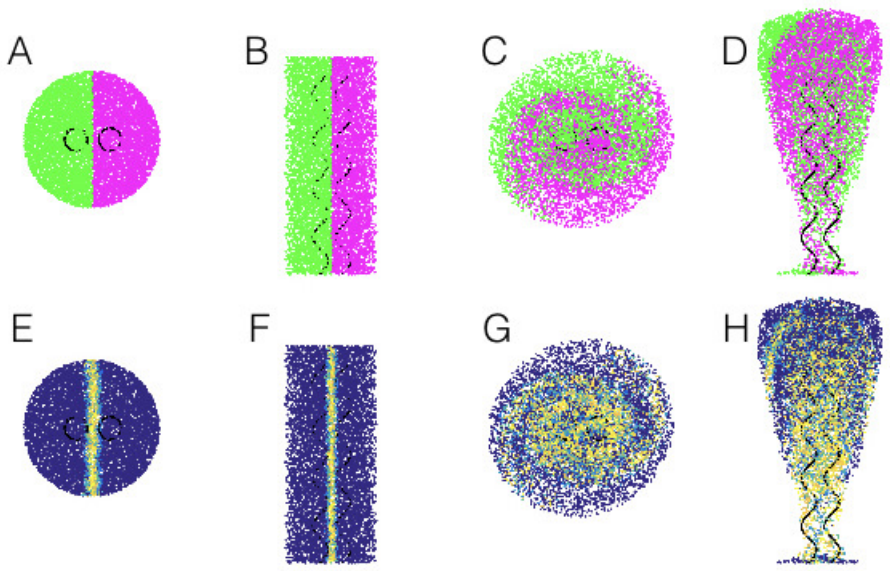

FIG. 10. Panels A and B show snapshots of particles seeded in a cylindrical region enclosing two identical helices at time $t = 0$ when viewed from (A) the top and (B) the side. Panels C and D show these same particles and the helices after twenty rotations. These helices are rotated in phase ($\phi = 0$) and are separated by a base distance of $d = 3\alpha = 0.255$. Panels E and F show the particles colored by their initial mixing measure $\hat{M}(p, 0)$. Panels G and H show these particles colored by their mixing measure $\hat{M}(p, 20)$ after twenty rotations. The mixing measure ranges from dark blue (no mixing) to yellow (optimal mixing).

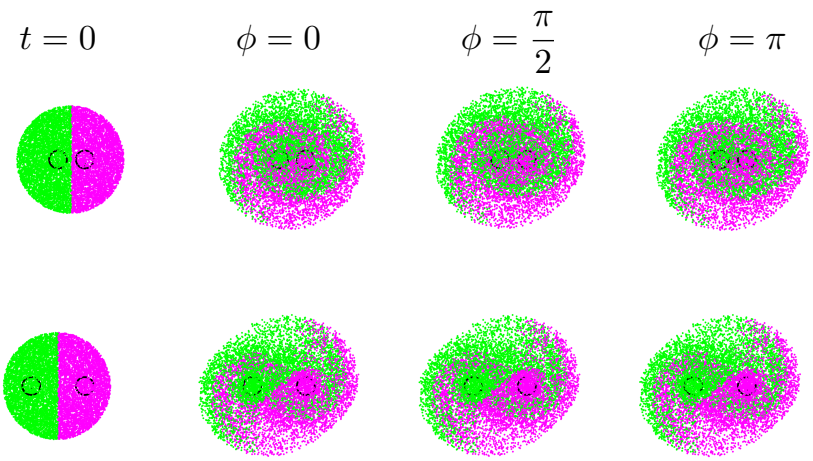

FIG. 11. Viewed from above, the first column shows the initial seeding of 5000 green and 5000 magenta particles, where each row depicts simulations with the same distance between helices ($d = 3\alpha$ (top) and 6α (bottom)). The phase difference between the helices is varied across columns ($\phi = 0$ (second column), $\phi = \pi/2$ (third column), and $\phi = \pi$ (fourth column)). The last three columns show the positions of the green and magenta particles after twenty rotations.

helix do not appear to mixing at all. This trend holds for $\phi = \pi/2$ (third column) and $\phi = \pi$ (fourth column) as well. We will quantify these observations using the mixing measures.

Figure 12 depicts the same simulations and same particle positions as in Figure 11, but now the particles are colored according to their mixing measures $\hat{M}(p, t)$. Visually, we observe the most mixing for the smallest separation distance, $d = 3\alpha$, where the yellow indicates regions of well-mixed particles in the center near the helices. When the spacing between helices is increased, the size of the regions with high mixing gets smaller. For $d = 6\alpha$, there are small, concentrated bands of well-mixed regions, but these coincide with the advection of the original border between the two particle types shown in the first column of Figure 11.

To further quantify the mixing at a time t, we average $\hat{M}(p, t)$ over all of the particles to give $M(t)$. We

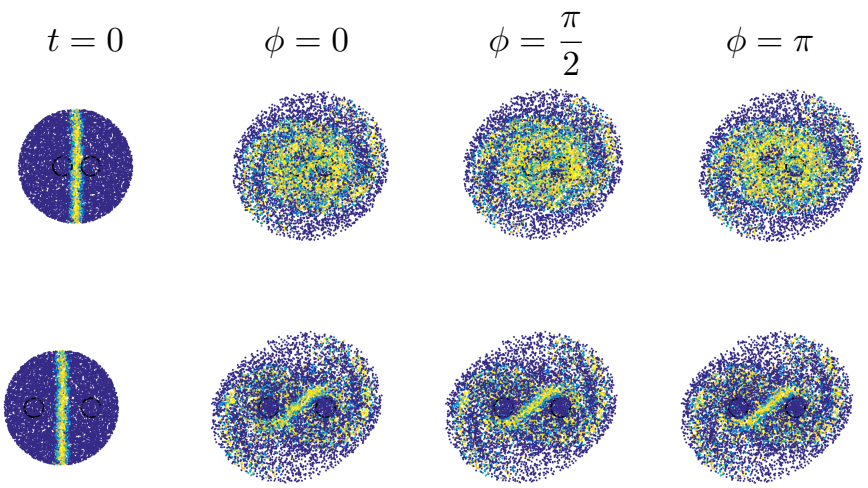

FIG. 12. Here the particles and helix configurations are the same as in Figure 11, but the particles are colored by their mixing measures. Viewed from above, the first column shows the initial seeding of the 10000 particles colored by their mixing measure $\hat{M}(p, 0)$, where each row depicts simulations with the same distance between helices ($d = 3\alpha$ (top) and 6α (bottom)). The phase difference between the helices is varied across columns ($\phi = 0$ (second column), $\phi = \pi/2$ (third column), and $\phi = \pi$ (fourth column)). The last three columns show the positions of the particles colored by their mixing measures $\hat{M}(p, 20)$ after twenty rotations.

performed twenty simulations, using five different phase differences and four distances between the helices. $M(t)$ is plotted as a function of helical rotations in Figure 13. Helical spacing is grouped by by line style, and the same phase difference is grouped by line color. When the separation distance is greatest (dotted lines), varying the phase difference has no effect. In addition, the least amount of mixing occurs during these simulations compared to the mixing computed for helices that are closer together. The overall trend we observe is that as the helices become closer together, there is both a larger mixing measure and a more prominent effect from varying phase difference. The maximal mixing, after 20 rotations, results from helices that are very close together and rotating completely out of phase.

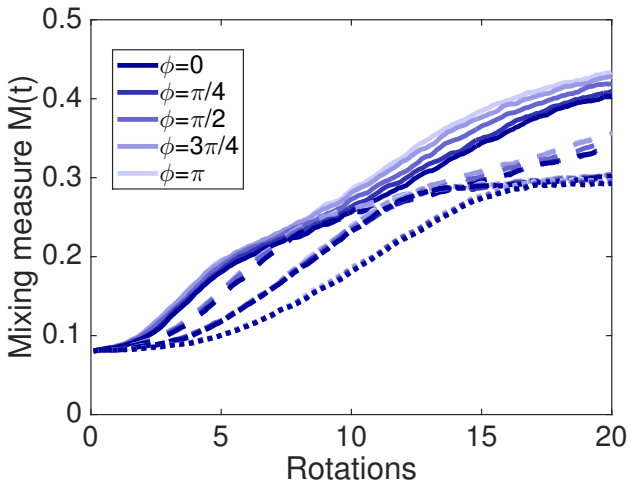

FIG. 13. Mixing as a function of number of helical rotations. Line style denotes helical spacing $d = 3\alpha$ (–), 4α (––), 5α (–·), 6α(· · ·) and color denotes phase difference ranging from in phase ($\phi = 0$ dark purple) to completely out of phase ($\phi = \pi$ light purple).

IV. CONCLUSION

We have investigated the fluid dynamics of a pair of rigid helices rotating at a constant velocity in a viscous fluid. We examined how the spacing between the helices and their phase difference influence their axial thrust and pumping ability. In essence, we have shown that the answer to the question "Are two helices twice as effective as one helix?" is "no". Two helices *close to one another* do not pump twice as much fluid across a flow meter as a single one, nor do they impart twice as much thrust. However, if the goal of these two helices is to mix their surrounding fluid, then our results suggest that they should be placed close together and rotated out of phase. While motivated by bacterical flagella, this study may have more direct implications in the design of fabricated helical rotors actuated in microfluidic environments, where precise geometries and rotation rates can be controlled, which is not possible in the world of biology.

Nevertheless, while the two-helix system studied here is certainly idealized, it is interesting to examine its relationship to the biological question of bacterial motility. The findings of the idealized system that two helices are *not* twice as effective as one is consistent with observa-

tions that bacteria with multiple flagella do not achieve greater swimming velocities than those with a single flagellum [15]. Moreover, the flagellar bundling model of Reigh et al. [15] demonstrate that tighter flagellar bundles enhance swimming efficiency compared to loosely bundled flagella, and that loosely bundled flagella are, in turn, not more efficient than an individual helix.

A similar idealized two helix system has previously been studied using a physical model that tracked velocities using PIV and a numerical model based upon slender body theory, all in free-space [29]. The studies presented here use a regularized Stokeslet formulation with images that accounts for the surface that the helices emanate from. By turning off the images, we see a significant change in flow features compared to those in the free-space idealization. Of course, we recognize that these calculations using images still represent an unbounded domain. Certainly, the flow generated by rotating helices in a microfluidic device is confined by more than one plane, as is the flow generated by nodal cilia during embryonic development [32]. We also offer these calculations as a caution and a reminder that using free-space solutions to quantify flow in a confined environment at the microscale only tells part of the story.

Acknowledgements

We thank Ricardo Cortez for helpful discussions. We also gratefully acknowledge the IMA supported program: WhAM! A Research Collaboration Workshop for Women in Applied Mathematics, Dynamical Systems with Applications to Biology and Medicine, where discussions of this work first began. Finally, the work of AB and LF was supported, in part, by NSF Grant DMS 1043626 and the work of KL was supported, in part, by NSF Grant DMS 1413078.

[1] E. Lauga, Annu. Rev. Fluid Mech. **48**, 105 (2016).
[2] N. Darnton, L. Turner, K. Breuer, and H. C. Berg, Biophys. J. **86**, 1863 (2004).
[3] M. Kim and K. Breuer, J. Fluids Engr. **129**, 319 (2007).
[4] L. Zhang, J. Abbott, L. Dong, K. E. Peyer, B. J. Kratochvil, H. Zhang, C. Bergeles, and B. J. Nelson, Nano Letters **9**, 3663 (2009).
[5] J. Gray and G. J. Hancock, J. Exp. Biol. **32**, 802 (1955).
[6] M. J. Lighthill, SIAM Review **18**, 161 (1976).
[7] R. Cortez, L. Fauci, and A. Medovikov, Phys. Fluids **17**, 031504 (2005).
[8] B. Rodenborn, C. Chen, H. Swinney, B. Liu, and H. P. Zhang, Proc. Natl. Acad. Sci. **110**, E338 (2012).
[9] J. T. Pham, A. Morozov, A. J. Crosby, A. Lindner, and O. du Roure, Phys. Rev. E **92**, 011004 (2015).
[10] M. Kim, J. C. Bird, A. J. Van Parys, K. S. Breuer, and T. R. Powers, Proc. Natl. Acad. Sci. **100**, 15481 (2003).
[11] H. Flores, E. Lobaton, S. Mendez-Diez, S. Tlupova, and R. Cortez, Bull. Math. Bio. **67**, 137 (2005).
[12] S. Lim and C. S. Peskin, Phys. Rev. E **85**, 036307 (2012).
[13] M. Reichert and H. Stark, Eur. Phys. J. E **17**, 493 (2005).
[14] P. Janssen and M. Graham, Phys. Rev. E **84**, 011910 (2011).
[15] S. Reigh, R. Winkler, and G. Gompper, Soft Matter **8**, 4363 (2012).
[16] E. Lauga, W. R. DiLuzio, G. M. Whitesides, and H. A. Stone, Biophys. J. **90**, 400 (2006).
[17] S. Zhong, K. Moored, V. Pinedo, J. Garcia-Gonzalez, and A. J. Smits, Exp. Therm. Fluid Sci. **46**, 1 (2013).
[18] M. J. Kim and T. R. Powers, Phys. Rev. E **69**, 061910 (2004).
[19] A. Buchmann, L. Fauci, K. Leiderman, E. Strawbridge, and L. Zhao, Appl. of Dynam. Systems in Biol. and Med.; IMA **158**, 35 (2015).
[20] J. D. Martindale, M. Jabbarzadeh, and H. C. Fu, Phys. Fluids **28**, 021901 (2016).
[21] S. Olson, S. Suarez, and L. Fauci, J. Theor. Biol. **283**, 203 (2011).
[22] J. Ainley, S. Durkin, R. Embid, P. Boindala, and R. Cortez, J. Comput. Phys. **227**, 4600 (2008).
[23] D. Smith, A. Smith, and J. Blake, J. Eng. Math **70**, 255 (2011).
[24] H. Guo and E. Kanso, Phys. Rev. E **93**, 033119 (2016).
[25] S. Olson and L. Fauci, Phys. Fluids **27**, 12901 (2015).
[26] S. Jung, K. Mareck, L. Fauci, and M. Shelley, Phys. of Fluids **19**, 103105 (2007).
[27] R. J. Cox, J. Fluid Mech. **44**, 791 (1970).
[28] *See Supplemental Material at [URL will be inserted by publisher] for movies of fluid particles in flow generated by two rotating helices.*
[29] M. J. Kim, M. J. Kim, J. C. Bird, J. Park, T. R. Powers, and K. S. Breuer, Exp. Fluids **37**, 782 (2004).
[30] J. R. Blake and A. T. Chwang, J. Engr. Math. **8**, 23 (1974).
[31] M. Robinson, P. Cleary, and J. Monaghan, AIChE journal **54**, 1987 (2008).
[32] S. Nonaka, H. Shiratori, Y. Saijoh, and H. Hamada, Nature **418**, 96 (2002).